

# Creep of stainless steel under heat flux cyclic loading (500-1000°C) with different mechanical preloads in a vacuum environment using 3D-DIC

Yong Su<sup>1,2a</sup>, Zhiwei Pan<sup>1b</sup>, Yongpei Peng<sup>1c</sup>, Shenghong Huang<sup>\*1</sup> and Qingchuan Zhang<sup>1\*\*</sup>

<sup>1</sup>CAS Key Laboratory of Mechanical Behavior and Design of Materials, Department of Modern Mechanics,  
University of Science and Technology of China, Hefei 230027, China  
<sup>2</sup>IAT-Chungu Joint Laboratory for Additive Manufacturing,  
Anhui Chungu 3D Printing Institute of Intelligent Equipment and Industrial Technology, Wuhu 241200, China

(Received June 11, 2019, Revised August 12, 2019, Accepted August 21, 2019)

**Abstract.** In nuclear fusion reactors, the key structural component (i.e., the plasma-facing component) undergoes high heat flux cyclic loading. To ensure the safety of fusion reactors, an experimental study on the temperature-induced creep of stainless steel under heat flux cyclic loading was performed in the present work. The strains were measured using a stereo digital image correlation technique (3D-DIC). The influence of the heat haze was eliminated, owing to the use of a vacuum environment. The specimen underwent heat flux cycles (500°C-1000°C) with different mechanical preloads (0 kN, 10 kN, 30 kN, and 50 kN). The results revealed that, for a relatively large preload (for example, 50 kN), a single temperature cycle can induce a residual strain of up to 15000  $\mu\epsilon$ .

**Keywords:** digital image correlation; nuclear fusion; high temperature measurement; creep; vacuum chamber

## 1. Introduction

Fusion power is an almost perfect energy source, owing to its abundance, sustainability, and low cost (Cowley 2016). In China, the *Experimental Advanced Superconducting Tokamak* (EAST) in Hefei has realized a stable steady-state high confinement plasma continued for 101.2 s. Correspondingly, the construction of the *China Fusion Engineering Test Reactor* (CFETR) will start in 2020 (Song *et al.* 2014). The *International Thermonuclear Experimental Reactor* (ITER) is being built in Europe, where realization of a *demonstration electricity-producing reactor* (DEMO) is projected for the 2040s (Romanelli *et al.* 2012). The hope is that, in the next 50 years, nuclear fusion energy will replace fossil fuels globally as the primary energy source.

After verification of the principles governing nuclear fusion, several key issues must be overcome for engineering realization of these principles. One of these issues is the sustainability of the *plasma-facing component* (PFC), i.e., a key component of nuclear fusion plants (Knaster *et al.* 2016). Located inside the annular vacuum chamber, PFC directly faces the plasma (operating temperature: hundreds of millions of degrees) and protects the peripheral

components and equipment from the impact of high heat flow and high-energy particle flow. The PFC undergoes *high heat flux loading* and, hence, an understanding of the component material behavior under high heat flux cyclic loading is critical (Linke *et al.* 1997, Arnoux *et al.* 2011, Wirtz *et al.* 2013).

This paper presents an experimental study on the creep of stainless steel under high flux cyclic loading. The *Digital image correlation* (DIC) technique was used to measure the strain at high temperature, owing to its attributes such as simple equipment, high measurement accuracy, and strong resistance to environmental noise (Yan *et al.* 2018, Zhang *et al.* 2018). This technique is used to find the same physical point in different images (Sutton *et al.* 2009, Xue *et al.* 2017, Aggelis *et al.* 2016). Employing blue light illumination and a band-pass filter, Grant *et al.* used the DIC method to measure the deformation occurring at temperatures of up to 1100 °C (Grant *et al.* 2009). Pan *et al.* fabricated a speckle pattern using cobalt oxide and measured the coefficient of thermal expansion corresponding to chromium-nickel austenitic stainless steel at 1200°C (Pan *et al.* 2011). Guo *et al.* used the DIC method to measure the elastic constants of graphite materials at 500°C (Guo *et al.* 2014). Using microscopic DIC, Chen *et al.* investigated the residual stress in thermal barrier ceramic coatings under thermal shock loading of 1100°C (Chen *et al.* 2014). Wu *et al.* developed an optical measurement system using 2D-DIC to evaluate the strain on the heated front surfaces of components at 1200°C (Wu *et al.* 2019). Hu *et al.* fabricated a speckle pattern via laser engraving and achieved satisfactory mechanical properties of the magnesium alloy exposed to high temperatures (Hu *et al.* 2018a, b). Ye *et al.* (2013, 2015, 2016a, b, 2017) have employed DIC technology for various studies that have

\*Corresponding author, Ph.D., Professor

E-mail: hshnpu@ustc.edu.cn

\*\* Ph.D., Professor

E-mail: zhangqc@ustc.edu.cn

<sup>a</sup> Ph.D.

<sup>b</sup> Ph.D. Student

<sup>c</sup> Ph.D. Student

included structural characterization and assessment. Nowadays, DIC is the strain metrology most widely used in high-temperature environments.

The application of the DIC method in high-temperature environments has been widely reported, but only a few reports have focused on the full-field measurement of *dynamic* thermal strains in high-temperature environments. Specifically, few studies have considered the residual strain associated with the working conditions (i.e., vacuum and high temperatures) of a nuclear fusion reactor. Hence, in this work, the application of the DIC method to temperature-induced creep is investigated.

This paper is organized as follows. Section 2 introduces the methods and principles. Sections 3, 4, 5, and 6 present the experimental procedures, experimental results, strain variation in an individual temperature cycle, and conclusions of this work, respectively.

## 2. Methods and principles

### 2.1 High heat flow comprehensive experimental platform

To investigate the material behavior in nuclear fusion environments, a *high heat flow comprehensive experimental platform* was established by Prof. Huang's Group at the University of Science and Technology of China with the support of CFETR. This platform consists of: a vacuum chamber, a commercial 3D-DIC system (PMLAB DIC-3D, Nanjing PMLAB Sensor Tech. Co., Ltd.), a mechanical loading system (30 kN for stretching and compression, 5 kNm for bending), an induction heating system (200 kW), a cooling circulation system (0-4 MPa, RT-200°C 7 m<sup>3</sup>/h), an electron gun (20 kW, 85 keV, 350 mA, scanning speed 10k), and a YAG high power laser (20 J/0.3<sup>-1</sup>ms). Equipped with multiple advanced measurement systems, this platform can simulate the cooling environment of nuclear fusion in service, can couple multiple loads (thermal/mechanical), and can be used for both material and component experiments. The establishment of this platform is the premise of current work.

### 2.2 Stereo digital image correlation technique

A stereo digital image correlation (3D-DIC) technique was employed to measure the full-field deformation of the specimen at high temperature. Previous studies including high-temperature deformation measurements are generally limited to the use of two-dimensional digital image correlation (2D-DIC) (Wang *et al.* 2015, Sakanashi *et al.* 2016, Valeri *et al.* 2017, Wang *et al.* 2017). Compared with 3D-DIC, 2D-DIC has several drawbacks: 1. a flat specimen is required for 2D-DIC; 2. for 2D-DIC, the optical axis must be perpendicular to the specimen (Xu *et al.* 2017a, Lv *et al.* 2018); 3. 2D-DIC is sensitive to out-of-plane deformation. Hence, if 3D-DIC is available, 3D-DIC (rather than 2D-DIC) should be used (Sutton *et al.* 2008).

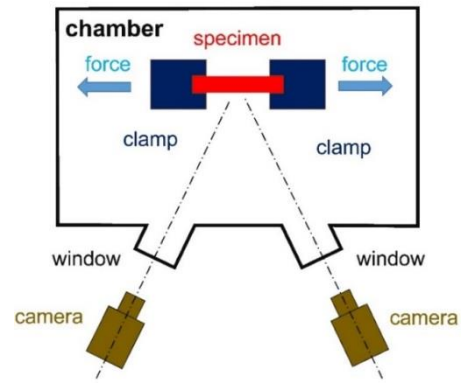


Fig. 1 Schematic of experimental setup. The vacuum chamber provides two observation windows for 3D-DIC

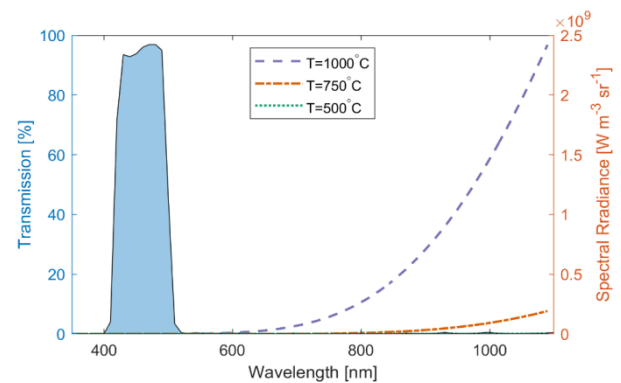


Fig. 2 Transmission of the band-pass filter and the spectral radiance calculated by Planck's law

To utilize 3D-DIC, the high heat flow comprehensive experimental platform provides two observation windows, as shown in Fig. 1. With two pre-calibrated cameras, the entire deformation field could be retrieved.

### 2.3 Pattern fabrication

The metrological performance of DIC is strongly dependent on the quality of the speckle pattern (Chen *et al.* 2018). The speckle pattern should be isotropic, uniform, and exhibit high image contrast (Sutton *et al.* 2009). Specifically, for high-temperature measurements, the speckle-making materials should be resistant to high temperatures and have good adhesion.

The speckle pattern was fabricated as follows. First, the white background was fabricated using a commercial ceramic coating material Pyro-Paint 634-AL (Aremco Products, Inc.). In general, the material is able to withstand temperatures of up to 1760°C. The paint Pyro-Paint 634-AL is composed of two ingredients: powder 634-AL-P and liquid 634-AL-L. The powder and liquid were mixed in a 3:1 ratio by weight. This mixture was then sprayed onto the specimen using a spray gun. Afterward, the specimen was dried at room temperature for 2 h, and then subjected to a heat cure at 93°C for 2 h. The black speckles were produced by HiE-Coat 840-C (Aremco Products, Inc.). According to the specifications, this material can resist temperatures of

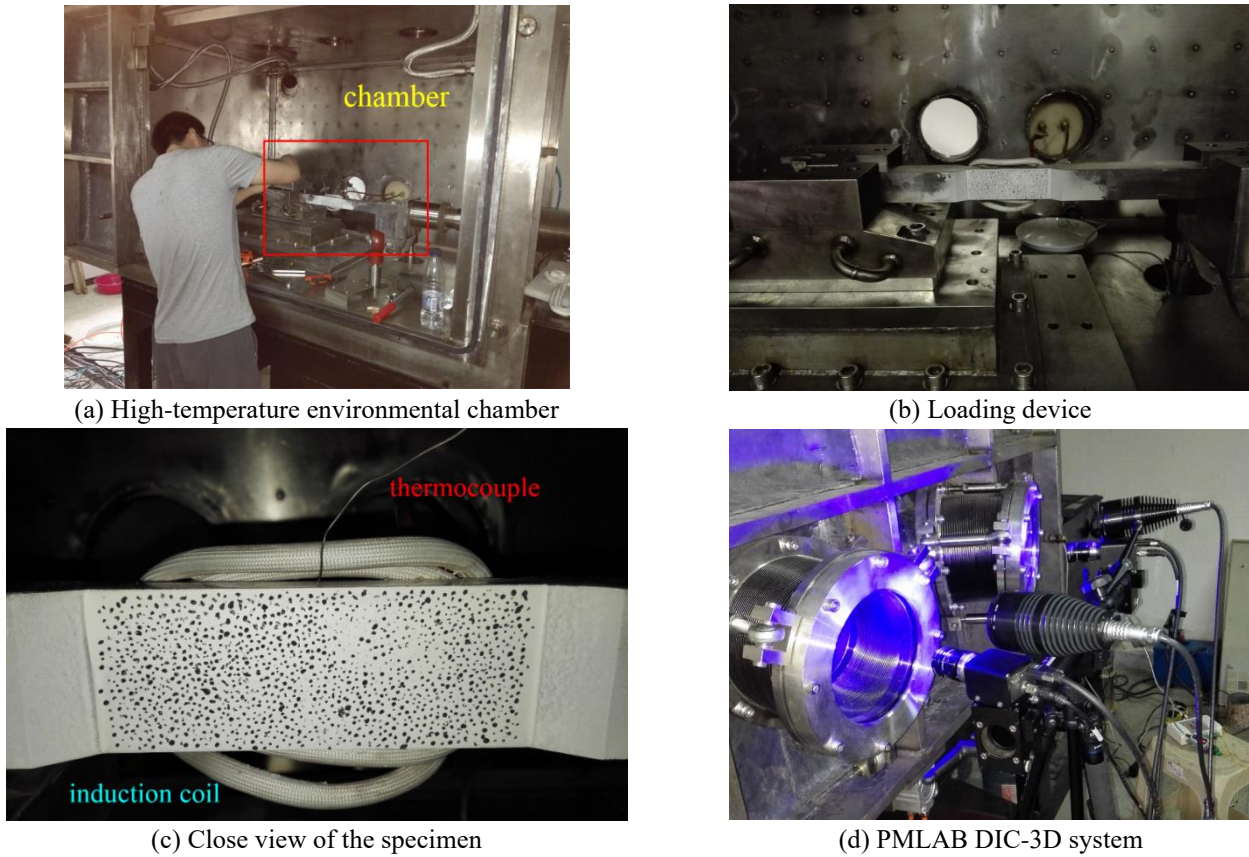


Fig. 3 Experimental set-up

up to 1371°C. HiE-Coat 840-C is a jet-black and water-based ceramic coating. The black coating material was transferred to the surface of the specimen using a pointed bamboo stick. The specimen was then dried at room temperature for 24 h.

#### 2.4 Filtering

At high temperature, the specimen will radiate visible light. Blue light (wavelength: 450 nm) and a band-pass filter (MID Opt BN470-30.5, Midwest Optical Systems, Inc.) were used to reduce the influence of radiation. The transmission of the optical filter is shown in Fig. 2.

According to Planck's equation, the spectral radiance is given as follows

$$B_{\lambda}(\lambda, T) = \frac{2hc^2}{\lambda^5} \frac{1}{\exp(hc / \lambda k_B T) - 1}, \quad (1)$$

Where,  $h$  is Planck's constant,  $c$  is the speed of light,  $k_B$  is Boltzmann's constant, and  $\lambda$  is the wavelength. The spectral radiance of different temperatures is shown in Fig. 2. When the temperature is lower than 1000°C, the filter can remove virtually all spectral radiance of the specimen.

### 3. Experiment

Inside the chamber, a stainless steel specimen was fixed

using two grips, as shown in Figs. 3(a) and 3(b). An induction coil, placed just behind the specimen, was used to heat the specimen; non-uniform heating of the specimen was expected, because the temperature distribution of the plasma-facing component is non-uniform in practical applications. The temperature was measured using a thermocouple, which was inserted into a hole drilled in the upper surface of the specimen (see Fig. 3(c) for a close view of the specimen; speckle size: ~9 pixels).

The door of the chamber was closed. A commercial 3D-DIC system (PMLAB DIC-3D, Nanjing PMLAB Sensor Tech. Co., Ltd.) was placed outside the chamber to measure the entire deformation field, as shown in Fig. 3(d). This 3D-DIC system consisted of two monochrome cameras (GRAS-50S5M/C, Point Grey Research, Inc., Resolution 2448×2048), two 23-mm prime lens (Schneider Optics, Inc.), two band-pass optical filters (MID Opt BN470-30.5, Midwest Optical Systems, Inc.), two blue light sources (PMLAB BLS), and a tripod (Manfrotto 161MK2B). An optical filter was mounted in front of each lens to filter out the black radiation of the specimen. The positions and directions of both cameras were carefully adjusted to maximize the specimen field of view. To reduce the influence of refraction, the optical axis of each camera was positioned perpendicular to the window (Gupta *et al.* 2014). Figure 4(a) shows the images acquired by the cameras.

The door of the chamber was opened. A calibration target, which is fabricated from aluminium foam, was used to calibrate the intrinsic and extrinsic parameters of the two

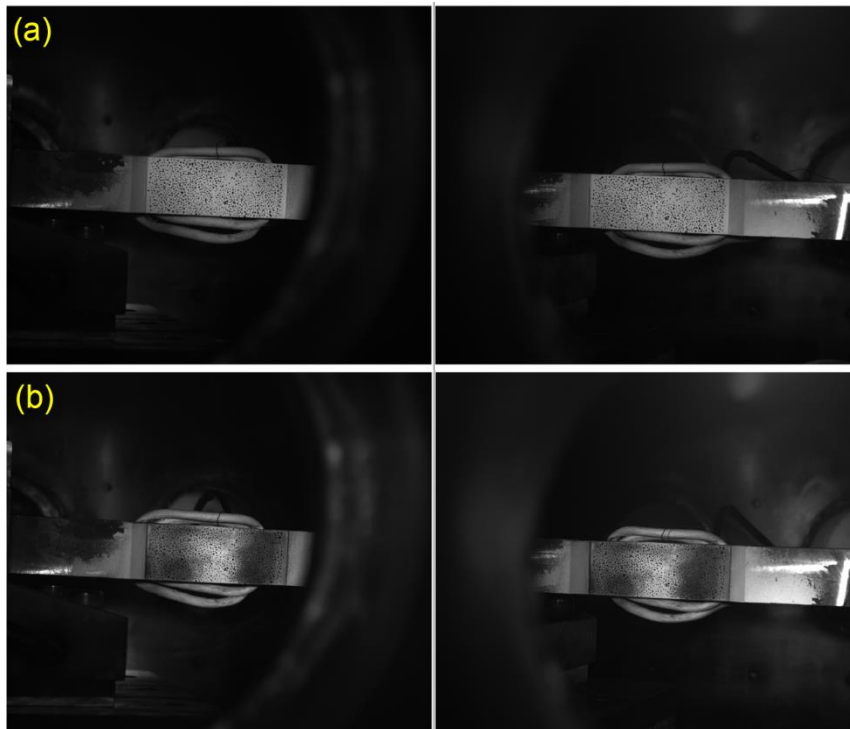


Fig. 4 Image (a) before and (b) after the pre-heating

cameras. The calibration target consists of a  $12 \times 9$  grid of circles, with a distance of 15 mm between successive circles. The calibration images were processed by the calibration module of the PMLAB DIC system (see Table 1 for the corresponding results). In Table 1,  $C_x$  and  $C_y$  denote the principal point;  $f_x$ ,  $f_y$ , and  $f_s$  represent focal lengths in unit of pixels;  $\alpha$ ,  $\beta$ , and  $\gamma$  represent the relative rotation of the two cameras;  $t_x$ ,  $t_y$ , and  $t_z$  represent the translation of the two cameras;  $k_1$  is the parameter describing the radial distortion of the lens (Gao *et al.* 2017, Zhang *et al.* 2018).

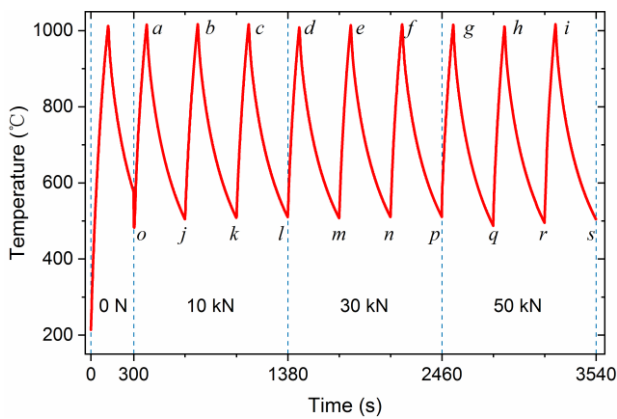
The door of the chamber was closed again and the chamber was sealed. The air was pumped out using a mechanical pump and an ion pump, and a vacuum of  $10^{-3}$  Pa was achieved. In such an environment, the thermal conductance was extremely small (Xiong *et al.* 2007, Cheng *et al.* 2008, Wu *et al.* 2013). In addition, the liquid cooling system was embedded in the observation window. The temperature rise of the observation window resulting from the thermal radiation was therefore extremely small and was unfelt by touch and, consequently, the refraction variation outside the chamber was marginal. Furthermore, usage of the vacuum environment eliminated the heat haze caused by refraction variation inside the chamber. In general, the influence of this variation (induced by high temperature) was reduced, owing to the vacuum environment.

Black precipitation appeared on the surface of the specimen after first heating and remained unchanged in the subsequent cycles. The chamber contained no air and, hence, this black substance resulted probably from the precipitation of carbon in stainless steel. This precipitation may cause pattern decorrelations, leading to significant deterioration in the measurement performance.

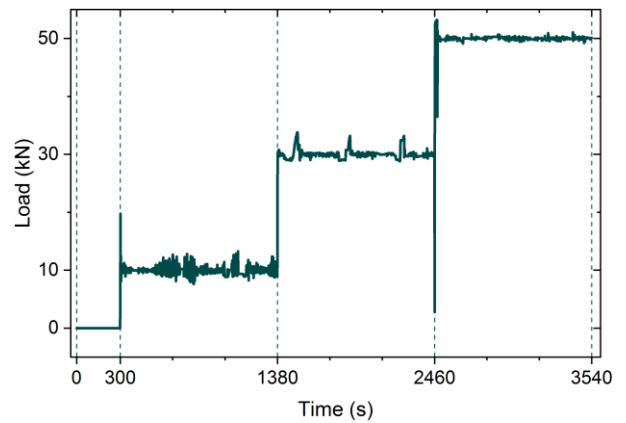
To tackle this issue, we introduced a pre-heating process, where the specimen was heated to  $1000^\circ\text{C}$  (see Fig. 4(b) for an image of the specimen after this process). The images that contain black precipitation were used as the reference images in the DIC analysis. Subsequently, the specimen was heated to simulate the heat flux associated with nuclear fusion. The specimen, with no mechanical load, was heated until the temperature reached  $1000^\circ\text{C}$ . Camera acquisition of the images was performed for 300 s at a rate of 1 frame/s. The loads (10 kN, 30 kN, and 50 kN) were then specified. For each mechanical load, three temperature cycles were conducted, where the specimen was heated to a temperature of  $1000^\circ\text{C}$  during each cycle.

Table 1 Calibration results of the measurement

parameter	left camera	right camera
$C_x$	1308.13 pixel	1198.62 pixel
$C_y$	1033.42 pixel	1027.15 pixel
$f_x$	6775.42 pixel	6683.69 pixel
$f_y$	6779.69 pixel	6685.22 pixel
$f_s$	1.43 pixel	-0.34 pixel
$\alpha$	0 rad	-0.01 rad
$\beta$	0 rad	0.55 rad
$\gamma$	0 rad	-0.01 rad
$t_x$	0 mm	-445.93 mm
$t_y$	0 mm	2.51 mm
$t_z$	0 mm	122.86 mm
$k_1$	-0.16	-0.18

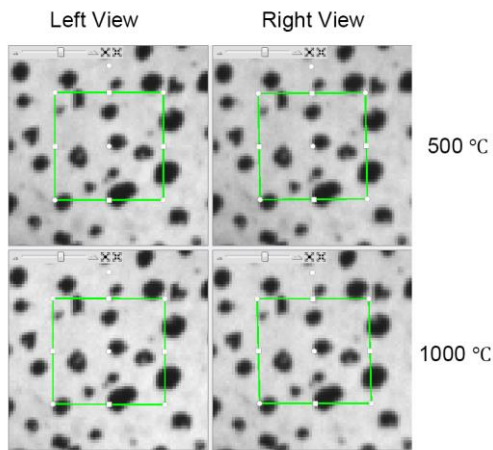


(a) Temperatures measured by the thermal couple



(b) Mechanical load determined by the sensor

Fig. 5 Temperature and mechanical-load variation with time

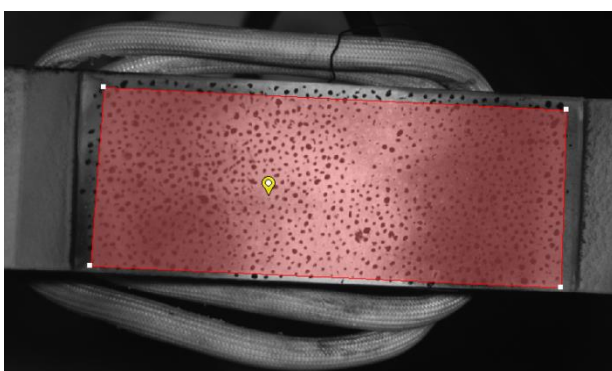


(a) Images obtained at 500°C and 1000°C

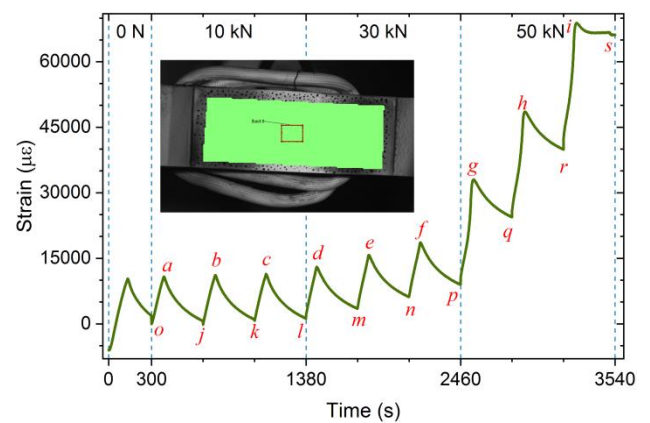


(b) The paint buckled in the final stages of the experiment

Fig. 6 The speckle pattern could tolerate high temperatures and finally failed via buckling



(a) Region of interest and the seed point



(b) The change of strain  $\epsilon_{xx}$  over time

Fig. 7 Region of interest and strains measured by DIC

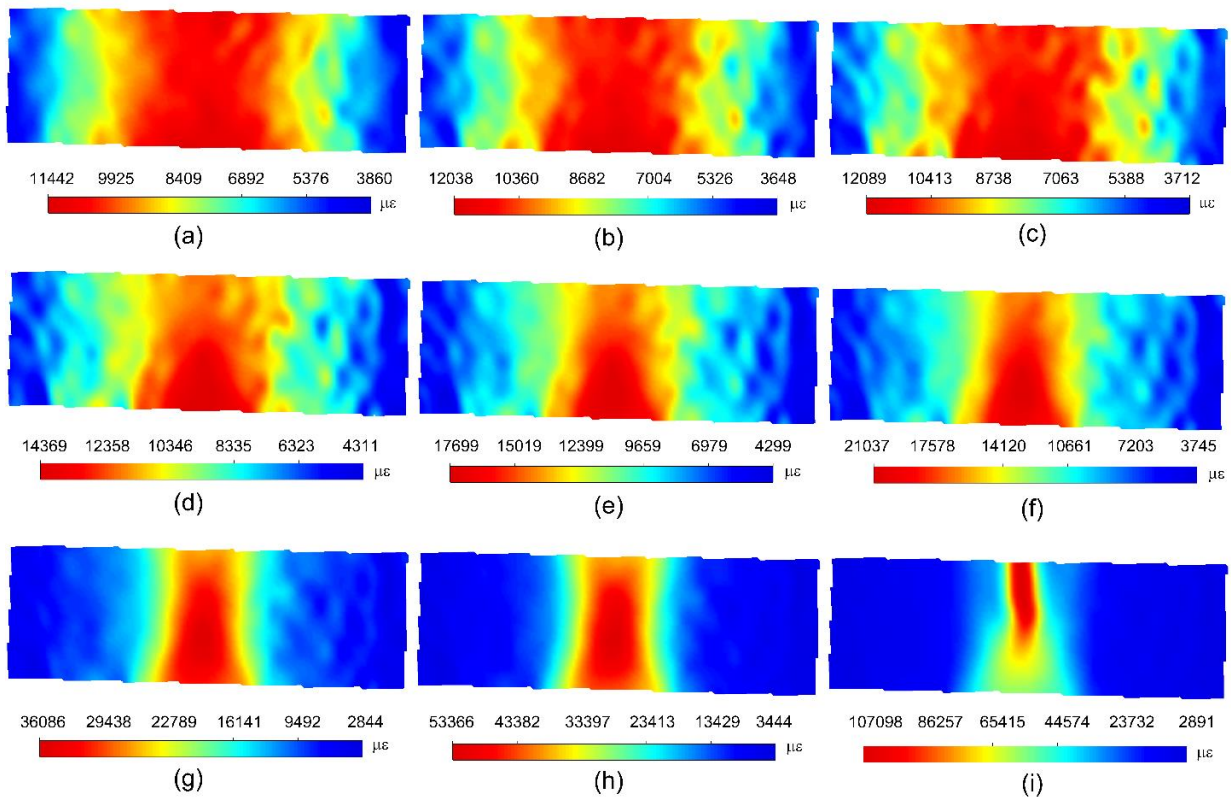


Fig. 8 Strain field of  $\varepsilon_{xx}$  at 1000 °C. The upper, middle, and lower rows correspond to mechanical preloads of 10 kN, 30 kN, and 50 kN, respectively, and the three columns correspond to three repetitions of each load

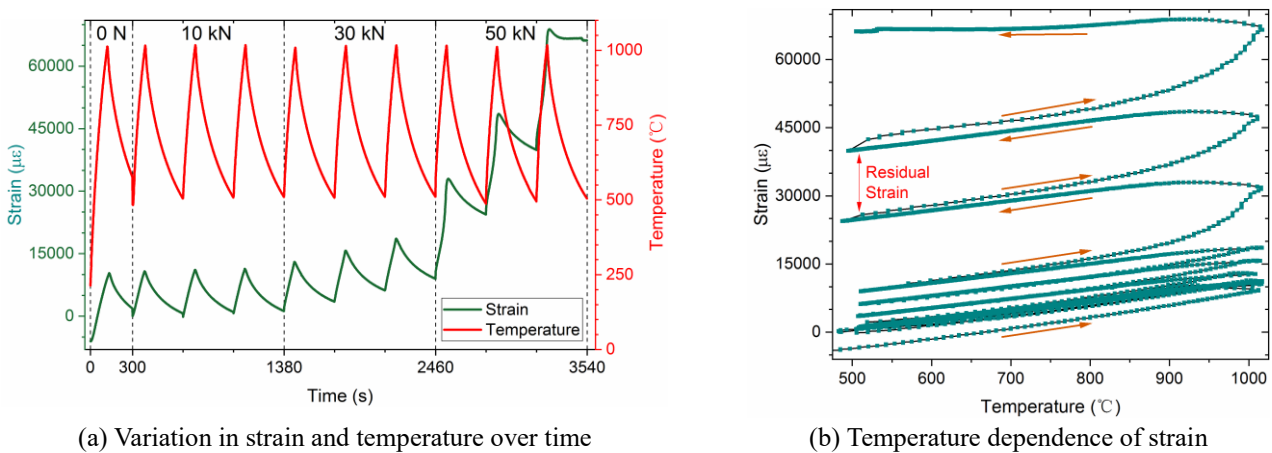


Fig. 9 Strain and temperature variation

Image acquisition started at a temperature of  $\sim 500$  °C and lasted for 360 s (see Table 2 for a summary of the image acquisition time and number of repetitions). The results in Figs. 5(a) and 5(b) show the temperature measured by the thermal couple (the heat flux is observed) and the mechanical loads, respectively.

Thanks to the blue light illumination and band-pass filter, the black radiation of the specimen was virtually eliminated. Fig. 6(a) shows the images obtained at 500°C and 1000°C. The good contrast of the speckle pattern was maintained even at a temperature of 1000°C. However, the fabricated speckle pattern buckled and, as shown in Fig. 6(b), was no longer adhered to the specimen surface in the final stages of the experiment.

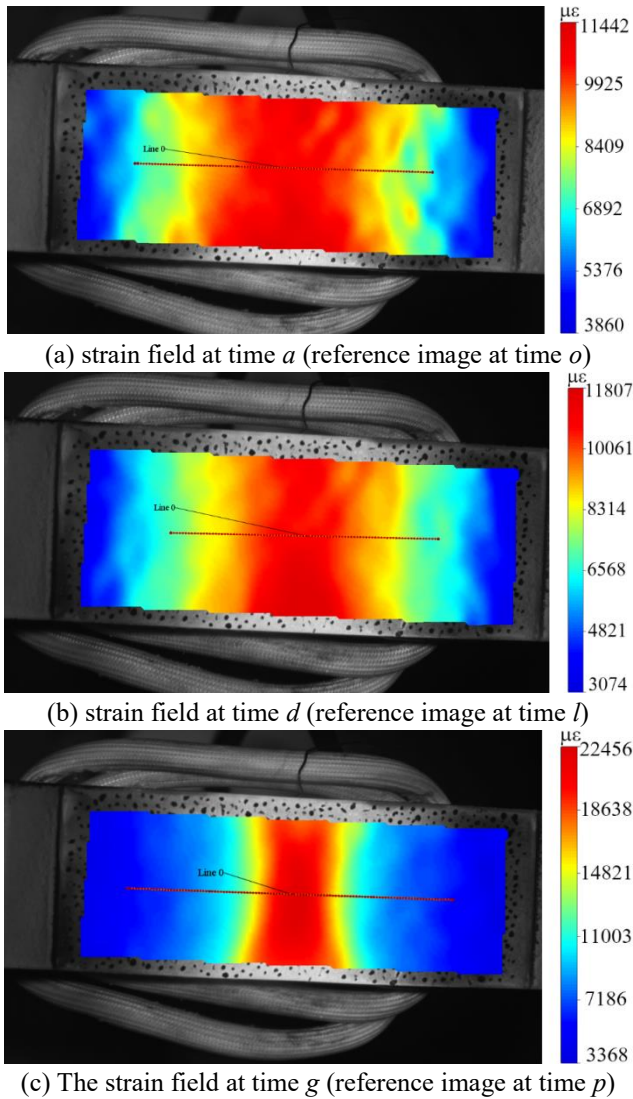


Fig. 10 Strain field at different times

Table 2 Image acquisition time and the numbers of repetitions

Load (kN)	Acquisition time (s)	Number of repetitions
0	300	1
10	360	3
30	360	3
50	360	3

#### 4. Results

The images were analyzed using the correlation module of commercial DIC system PMLAB DIC-3D. The region of interest and the seed point are shown in Fig. 7(a). In this work, we focus on the creep under mechanical preloads and, hence, the images at time  $o$  (see Fig. 5(a)) are selected as the reference images; that is, the strain at time  $o$  is

regarded as zero. The grid step, subset size, and boundary validation are 5 pixels, 39 pixels, and 80%, respectively. PMLAB DIC-3D utilizes a modified version of the inverse compositional Gauss-Newton method for subpixel registration (Gao *et al.* 2015, Shao *et al.* 2015). The interpolation algorithm is a bi-cubic B-spline (Pan *et al.* 2016, Gao *et al.* 2016, Liu *et al.* 2019). In addition, a first-order shape function is employed (Xu *et al.* 2015, 2017b) and the similarity is characterized via the zero-mean normalized sum of squared difference.

Fig. 8 illustrates the strain field  $\epsilon_{xx}$  calculated via 3D-DIC at 1000°C. The results shown in Figs. 8(a)-8(i) correspond to times  $a-i$ , respectively, in Fig. 5(a). The results corresponding to mechanical preloads of 10 kN, 30 kN, and 50 kN are shown in the top, middle, and bottom rows, respectively, and the three columns correspond to the three repetitions of each loading. As Fig. 8 shows, with increasing mechanical preload, the strain increases and the deformation becomes increasingly localized. The strain in Fig. 8(i) is non-symmetric, as evidenced by buckling of the paint (see Fig. 6(b)). To analyze the strain, a rectangular region is chosen and the average strain inside this region is determined (see Fig. 7(b)). The results reveal that the residual strain increases with increasing mechanical preload, and is quite significant at a preload of 50 kN.

The mechanical load is time dependent, as shown in Fig. 5(b). Nevertheless, the influence of the mechanical-load variation is negligible, because the thermally induced strain is considerably larger than the mechanically induced strain. For example, at time  $t=1380$  s, the mechanical load increases by 20 kN and, hence, the strain is discontinuous and increases (see Fig. 7(b)). This increase is, however, relatively small compared with the thermally induced strain; since the variation in the mechanical load is  $\ll 20$  kN, the influence of this variation could be ignored.

Changes in the temperature and strain over time are further investigated by combining Figs. 5(a) and 7(b) into Fig. 9(a). Fig. 9(b) shows the temperature dependence of the strain. When the mechanical preload is relatively small, the residual strain is negligible, whereas for a relatively large preload (e.g., 50 kN), the residual strain is quite significant.

#### 5. Discussion

The evolution of deformation in an individual heat cycle is evaluated by analyzing the deformations in cycles  $o-a-j$ ,  $l-d-m$ , and  $p-g-q$  (see Fig. 7(b)), corresponding to mechanical loads of 10kN, 30kN, and 50kN, respectively.

The temperature cycle  $o-a-j$  corresponds to a mechanical preload of 10 kN. The maximal temperature occurs at time  $a$ , i.e., 91 s after time  $o$ . Fig. 10(a) shows the strain field at time  $a$ . The strain variation is illustrated (see Figs. 11(a) and 11(b)) by extracting the strains along the line shown in Fig. 10(a). The plots in Figs. 11(a) and 11(b) show the strains generated during the  $o-a$  heating process and the strain occurring at the end of the process, respectively. During heating, the strains at the center are larger than those at the two sides, and the maximal strain is  $\sim 11000 \mu\epsilon$ .

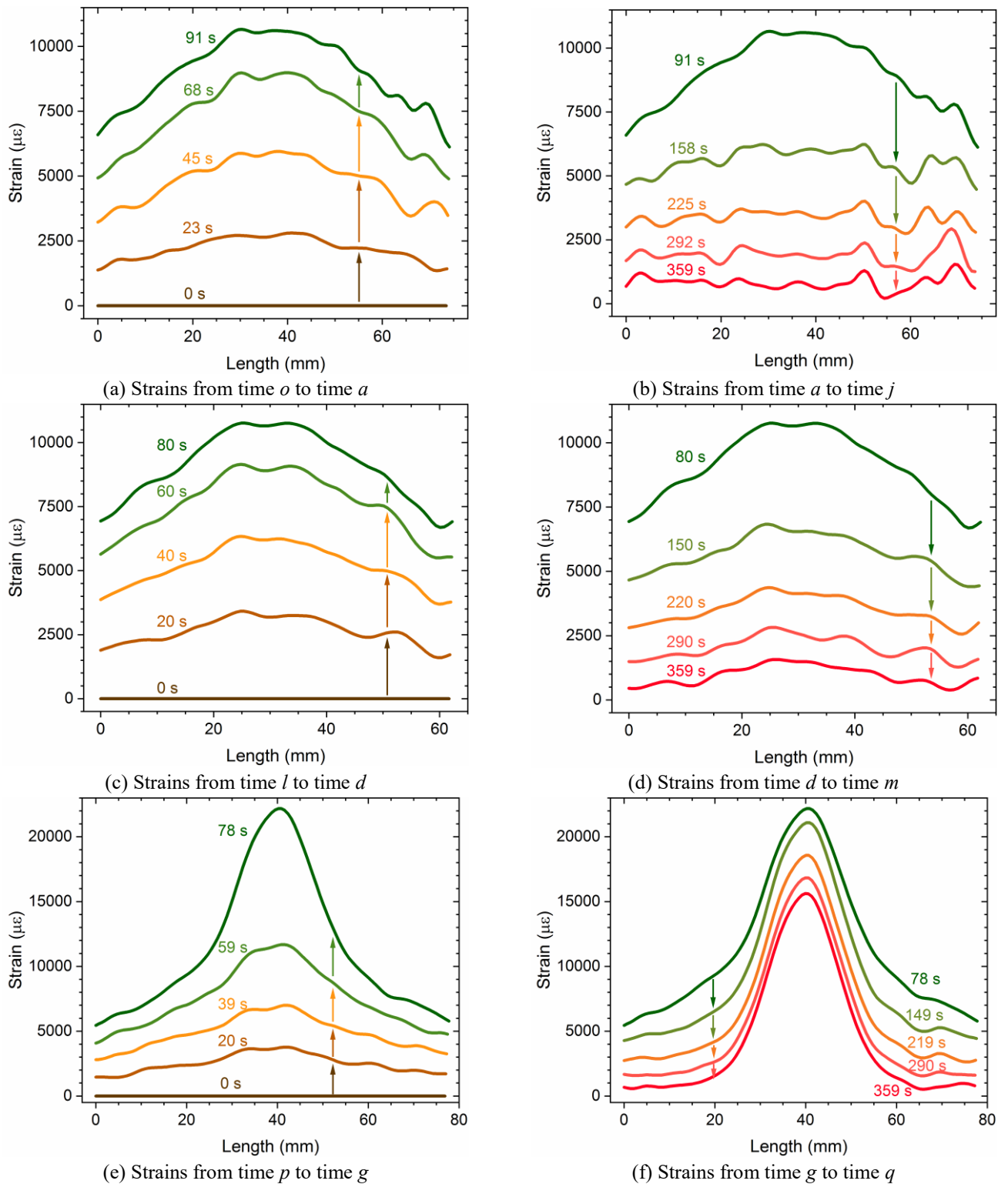


Fig. 11 Strains at different temperature cycles

The heat cycle  $l$ - $d$ - $m$  corresponds to a preload of 30 kN. Therefore, the image at time  $l$  is set as the new reference image. The 360 images obtained for cycle  $l$ - $d$ - $m$  are recalculated using the previously employed calculation parameters. Moreover, the maximal temperature occurs at time  $d$ , i.e., 80 s after time  $l$ . Fig. 10(b) shows the strain

field at time  $d$ . The deformation shown in Fig. 10(b) is relative to time  $l$ , because the reference image was acquired at time  $l$ . The strains along the line shown in Fig. 10(b) are extracted and are shown in Figs. 11(c) and 11(d). The maximal strain,  $\sim 11000 \mu\epsilon$ , is approximately the same as that determined for the 10 kN preload.

The heat cycle  $p$ - $g$ - $q$  corresponds to a preload of 50 kN. The image at time  $p$  is set as the new reference image, and the images in cycle  $p$ - $g$ - $q$  are recalculated. Furthermore, the maximal temperature occurred at time  $g$ , i.e., 78 s after time  $p$ . Fig. 10(c) shows the strain field at time  $g$ , where the reference image is obtained at time  $p$  and the deformation shown corresponds to this time. The strains along the line shown in Fig. 10(c) are extracted and are depicted in Figs. 11(e) and 11(f). The maximal strain is  $\sim 22000 \mu\epsilon$ , which is considerably larger than the strain associated with loads of 10 kN and 30 kN. Moreover, the deformation becomes quite localized, and a maximum residual strain of  $15000 \mu\epsilon$  is noted.

Movies showing the evolution of the deformation can be found in an open digital library (Su 2019).

## 6. Conclusions

Full-field measurements of thermally induced creep are essential for structural materials exposed to the working conditions associated with nuclear fusion reactors. In this work, the temperature-induced creep of stainless steel under heat flux cyclic loading with different mechanical preloads in a vacuum environment was experimentally evaluated using 3D-DIC. The influence of the heat haze was eliminated, owing to the use of the vacuum environment. Compared with 2D-DIC, the 3D-DIC technique used in this work exhibited superior measurement performance. With different mechanical preloads (0 kN, 10 kN, 30 kN, and 50 kN), the specimen underwent heat flux cycles from 500°C to 1000°C.

The full-field deformations caused by the mechanical and thermal loads were measured. The results revealed that for a relatively large preload (e.g., 50 kN), the residual strain induced by heat flux cyclic loading is quite significant, reaching levels of up to  $15000 \mu\epsilon$ . To the authors' knowledge, this is the first experimental study employing 3D-DIC for full-time strain measurements under heat flux cyclic loading with different mechanical preloads.

The novelty of this paper is as follows: (1) the emergence and the evolution of a full-field thermally induced residual strain was measured using 3D-DIC; (2) the residual strain increased significantly and became quite localized when the mechanical preload exceeded a certain value (for example, 50 kN).

## Acknowledgments

This work is supported by the National Natural Science Foundation of China (Grant Nos. 11627803, 11702287, 11872354), the National Magnetic Confinement Fusion Science Program of China (Grants Nos. 2015GB121007), the Strategic Priority Research Program of the Chinese Academy of Sciences (XDB22040502), and the Fundamental Research Funds for the Central Universities (WK2480000004).

## References

- Aggelis, D.G., Verbruggen, S., Tsangouri, E., Tysmans, T. and Van Hemelrijck, D. (2016), "Monitoring the failure mechanisms of a reinforced concrete beam strengthened by textile reinforced cement using acoustic emission and digital image correlation", *Smart. Struct. Syst.* **17**(1), 91-105. <https://doi.org/10.12989/sss.2016.17.1.091>.
- Arnoux, G., Bazylev, B., Lehnen, M., Loarte, A., Riccardo, V., Bozhenkov, S., Devaux, S., Eich, T., Fundamenski, W., Hender, T., Huber, A., Jachmich, S., Kruezi, U., Sergienko, G. and Thomsen, H. (2011). "Heat load measurements on the JET first wall during disruptions", *J. Nucl. Mater.* **415**(1), S817-S820. DOI: 10.1016/j.jnucmat.2010.11.042.
- Chen, X.M., Liu, Z.W. and Yang Y. (2014). "Residual stress evolution regularity in thermal barrier coatings under thermal shock loading", *Theor. Appl. Mech. Lett.* **4**(2), 021009. DOI: 10.1063/2.1402109.
- Chen, Z.N., Shao, X.X., Xu, X.Y. and He, X.Y. (2018). "Optimized digital speckle patterns for digital image correlation by consideration of both accuracy and efficiency", *Appl. Opt.* **57**(4), 884-893. DOI: 10.1364/AO.57.000884.
- Cheng, T., Zhang, Q.C., Wu, X.P., Chen, D.P. and Jiao, B.B. (2008). "Uncooled infrared imaging using a substrate-free focal-plane array", *IEEE Electron Device Lett.* **29**(11), 1218-1221. DOI: 10.1109/LED.2008.2004568.
- Cowley, S.C. (2016), "The quest for fusion power", *Nat. Phys.*, **12**, 384. DOI: 10.1038/nphys3719.
- Gao, Y., Cheng, T., Su, Y., Xu, X.H., Zhang, Y. and Zhang, Q.C. (2015), "High-efficiency and high-accuracy digital image correlation for three-dimensional measurement", *Opt. Lasers Eng.*, **65**, 73-80. DOI: 10.1016/j.optlaseng.2014.05.013.
- Gao, Z.R., Xu, X.H., Su, Y. and Zhang, Q.C. (2016), "Experimental analysis of image noise and interpolation bias in digital image correlation", *Opt. Lasers Eng.*, **81**, 46-53. DOI: 10.1016/j.optlaseng.2016.01.002.
- Gao, Z.R., Zhang, Q.C., Su, Y. and Wu, S.Q. (2017), "Accuracy evaluation of optical distortion calibration by digital image correlation", *Opt. Lasers Eng.*, **98**, 143-152. DOI: 10.1016/j.optlaseng.2016.01.002.
- Grant, B.M.B., Stone, H.J., Withers, P.J. and Preuss, M. (2009), "High-temperature strain field measurement using digital image correlation", *J. Strain Anal. Eng. Des.*, **44**(4), 263-271. DOI: 10.1243/03093247JSA478.
- Guo, B.Q., Wang, H.X., Xie, H.M. and Chen, P.W. (2014), "Elastic constants characterization on graphite at 500°C by the virtual fields method", *Theor. Appl. Mech. Lett.*, **4**(2), 021010. DOI: 10.1063/2.1402110.
- Gupta, S., Parameswaran, V., Sutton, M.A. and Shukla, A. (2014). "Study of dynamic underwater implosion mechanics using digital image correlation", *Proc. R. Soc. A-Math. Phys. Eng. Sci.*, **470**(2172), 20140576-20140576. DOI: 10.1098/rspa.2014.0576.
- Hu, Y.J., Wang, Y.J., Chen, J.B. and Zhu, J.M. (2018a), "A new method of creating high-temperature speckle patterns and its application in the determination of the high-temperature mechanical properties of metals", *Exp. Tech.*, **42**(5), 523-532. DOI: 10.1007/s40799-018-0256-z.
- Hu, Y.J., Liu, F., Zhu, W.D. and Zhu, J.M. (2018b). "Thermally coupled constitutive relations of thermoelastic materials and determination of their material constants based on digital image correlation with a laser engraved speckle pattern", *Mech. Mat.* **121**, 10-20. DOI: 10.1016/j.mechmat.2018.02.002.
- Knaster, J., Moeslang, A. and Muroga, T. (2016), "Materials research for fusion", *Nat. Phys.*, **12**, 424. DOI: 10.1038/NPHYS3735.
- Linke, J., Akiba, M., Bolt, H., Breitbach, G., Duwe, R.,

- Makhankov, A., Ovchinnikov, I., Rodig, M. and Wallura, E. (1997), "Performance of beryllium, carbon, and tungsten under intense thermal fluxes", *J. Nucl. Mater.*, **241**, 1210-1216. DOI: 10.1016/S0022-3115(97)80222-X.
- Liu, Y., Zhang, Q.C., Su, Y., Gao, Z.R., Fang, Z. and Wu, S.Q. (2019), "The mechanism of strain influence on interpolation induced systematic errors in digital image correlation method", *Opt. Lasers Eng.*, **121**, 323-333. DOI: 10.1016/j.optlaseng.2019.04.023.
- Lv, Z.Q., Xu, X.H., Yan, T.H., Cai, Y.L., Su, Y. and Zhang, Q.C. (2018), "High-accuracy optical extensometer based on coordinate transform in two-dimensional digital image correlation", *Opt. Lasers Eng.*, **100**, 61-70. DOI: 10.1016/j.optlaseng.2017.06.010.
- Pan, B., Wu, D.F., Wang, Z.Y. and Xia, Y. (2011), "High-temperature digital image correlation method for full-field deformation measurement at 1200°C", *Meas. Sci. Technol.*, **22**(1), 015701. DOI: 10.1088/0957-0233/22/1/015701.
- Pan, Z., Chen, W., Jiang, Z.Y., Tang, L.Q., Liu, Y.P. and Liu, Z.J. (2016), "Performance of global look-up table strategy in digital image correlation with cubic B-spline interpolation and bicubic interpolation", *Theor. Appl. Mech. Lett.*, **6**(3), 126-130. DOI: 10.1016/j.taml.2016.04.003.
- Romanelli, F., Barabaschi, P., Borba, D., Federici, G., Horton, L., Neu, R., Stork, D. and Zohm, H. (2012), "Fusion electricity: a roadmap to the realization of fusion energy".
- Sakanashi, Y., Gungor, S., Forsey, A.N. and Bouchard, P. J. (2016), "Measurement of creep deformation across welds in 316h stainless steel using digital image correlation", *Exp. Mech.*, **57**(2), 231-244. DOI: 10.1007/s11340-016-0245-z.
- Shao, X.X., Dai, X.J. and He, X.Y. (2015), "Noise robustness and parallel computation of the inverse compositional Gauss-Newton algorithm in digital image correlation", *Opt. Lasers Eng.*, **71**, 9-19. DOI: 10.1016/j.optlaseng.2015.03.005.
- Song, Y.T., Wu, S.T., Li, J.G., Wan, B.N., Wan, Y.X., Fu, P., Ye, M.Y., Zheng, J.X., Lu, K., Gao, X.G., Liu, S.M., Liu, X.F., Lei, M.Z., Peng, X.B. and Chen, Y. (2014), "Concept design of CFETR Tokamak machine", *IEEE T. Plasma Sci.*, **42**(3), 503-509. DOI: 10.1109/TPS.2014.2299277.
- Su, Y. (2019), "Creep of stainless steel under heat flux cyclic loading (500-1000°C) using 3D-DIC", figshare [retrieved 17 Jul 2019], DOI: 10.6084/m9.figshare.8940341.v1.
- Sutton, M.A., Yan, J.H., Tiwari, V., Schreier, H.W. and Orteu, J.J. (2008), "The effect of out-of-plane motion on 2D and 3D digital image correlation measurements", *Opt. Lasers Eng.*, **46**(10), 746-757. DOI: 10.1016/j.optlaseng.2008.05.005.
- Sutton, M.A., Schreier, H.W. and Orteu, J.J. (2009), *Image Correlation for Shape, Motion and Deformation Measurements: Basic Concepts, Theory and Applications*, Springer Publishing Company, Incorporated. DOI: 10.1007/978-0-387-78747-3.
- Valeri, G., Koohbor, B., Kidane, A. and Sutton, M.A. (2017), "Determining the tensile response of materials at high temperature using DIC and the Virtual Fields Method", *Opt. Lasers Eng.*, **91**, 53-61. DOI: 10.1016/j.optlaseng.2016.11.004.
- Wang, S., Yao, X.F., Su, Y.Q. and Ma, Y.J. (2015), "High temperature image correction in DIC measurement due to thermal radiation", *Meas. Sci. Technol.* **26**(9), 095006. DOI: 10.1088/0957-0233/26/9/095006.
- Wang, W., Xu, C.H., Jin, H., Meng, S.H., Zhang, Y.M. and Xie, H.W. (2017), "Measurement of high temperature full-field strain up to 2000 °C using digital image correlation", *Meas. Sci. Technol.*, **28**(3), 035007. DOI: 10.1088/1361-6501/aa56d1.
- Wirtz, M., Linke, J., Pintsuk, G., De Temmerman, G. and Wright, G.M. (2013), "Thermal shock behaviour of tungsten after high flux H-plasma loading", *J. Nucl. Mater.*, **443**(1-3), 497-501. DOI: 10.1016/j.jnucmat.2013.08.002.
- Wu, D.F., Lin, L.J., Ren, H.Y., Zhu, F.H. and Wang, H.T. (2019), "High-temperature deformation measurement of the heated front surface of hypersonic aircraft component at 1200°C using digital image correlation", *Opt. Lasers Eng.* **122**: 184-194. DOI: 10.1016/j.optlaseng.2019.06.006.
- Wu, J.X., Cheng, T., Zhang, Q.C., Zhang, Y., Mao, L., Gao, J., Chen, D.P. and Wu X.P. (2013), "Research of infrared imaging at atmospheric pressure using a substrate-free focal plane array", *Chin. Phys. Lett.*, **30**(1), 010701. DOI: 10.1088/0256-307X/30/1/010701.
- Xiong, Z.M., Zhang, Q.C., Gao, J., Wu, X.P., Chen, D.P. and Jiao, B.B. (2007), "The pressure-dependent performance of a substrate-free focal plane array in an uncooled infrared imaging system", *J. Appl. Phys.*, **102**(11), 113524. DOI: 10.1063/1.2822333.
- Xu, X.H., Su, Y., Cai, Y.L., Cheng, T. and Zhang, Q.C. (2015), "Effects of various shape functions and subset size in local deformation measurements using DIC", *Exp. Mech.*, **55**(8), 1575-1590. DOI: 10.1007/s11340-015-0054-9.
- Xu, X.H., Zhang, Q.C., Su, Y., Cai, Y.L., Xue, W.W., Gao, Z.R., Xue, Y., Lv, Z.Q. and Fu, S.H. (2017a), "High-accuracy, high-efficiency compensation method in two-dimensional digital image correlation", *Exp. Mech.*, **57**(6), 831-846. DOI: 10.1007/s11340-017-0274-2.
- Xu, X.H., Su, Y. and Zhang, Q.C. (2017b), "Theoretical estimation of systematic errors in local deformation measurements using digital image correlation", *Opt. Lasers Eng.*, **88**, 265-279. DOI: 10.1016/j.optlaseng.2016.08.016.
- Xue, Y., Su, Y., Zhang, C., Xu, X.H., Gao, Z.R., Wu, S.Q., Zhang, Q.C. and Wu, X.P. (2017), "Full-field wrist pulse signal acquisition and analysis by 3D digital image correlation", *Opt. Lasers Eng.*, **98**, 76-82. DOI: 10.1016/j.optlaseng.2017.05.018.
- Yan, T.H., Su, Y. and Zhang, Q.C. (2018), "Precise 3D shape measurement of three-dimensional digital image correlation for complex surfaces", *Sci. China-Technol. Sci.*, **61**(1), 68-73. DOI: 10.1007/s11431-017-9125-7.
- Ye, X.W., Ni, Y.Q., Wai, T.T., Wong, K.Y., Zhang, X.M. and Xu, F. (2013), "A vision-based system for dynamic displacement measurement of long-span bridges: algorithm and verification", *Smart. Struct. Syst.*, **12**(3-4), 363-379. [https://doi.org/10.12989/sss.2013.12.3\\_4.363](https://doi.org/10.12989/sss.2013.12.3_4.363).
- Ye, X.W., Yi, T.H., Wen, C. and Su, Y.H. (2015), "Reliability-based assessment of steel bridge deck using a mesh-insensitive structural stress method", *Smart. Struct. Syst.*, **16**(2), 367-382. <https://doi.org/10.12989/sss.2015.16.2.367>.
- Ye, X.W., Dong, C.Z. and Liu, T. (2016a), "Image-based structural dynamic displacement measurement using different multi-object tracking algorithms", *Smart. Struct. Syst.*, **17**(6), 935-956. <https://doi.org/10.12989/sss.2016.17.6.935>.
- Ye, X.W., Dong, C.Z. and Liu, T. (2016b), "Force monitoring of steel cables using vision-based sensing technology: methodology and experimental verification", *Smart. Struct. Syst.*, **18**(3), 585-599. <https://doi.org/10.12989/sss.2016.18.3.585>.
- Ye, X.W., Yi, T.H., Su, Y.H., Liu, T. and Chen, B. (2017), "Strain-based structural condition assessment of an instrumented arch bridge using FBG monitoring data", *Smart. Struct. Syst.*, **20**(2), 139-150. <https://doi.org/10.12989/sss.2017.20.2.139>.
- Zhang, X., Su, Y., Gao, Z.R., Xu, T., Ding, X.H., Yu, Q.F. and Zhang, Q.C. (2018), "High-accuracy three-dimensional shape measurement of micro solder paste and printed circuits based on digital image correlation", *Opt. Eng.*, **57**(5), 054101. DOI: 10.1117/1.OE.55.5.054101.